Journal of Nuclear Materials 528 (2020) 151876

Contents lists available at ScienceDirect

Journal of Nuclear Materials

journal homepage: www.elsevier.com/locate/jnucmat

Thermophysical properties of urania-zirconia $(U,Zr)O_2$ mixed oxides by molecular dynamics

D.G. Frost [a, b], C.O.T. Galvin [a], M.W.D. Cooper [c], E.G. Obbard [a, b], P.A. Burr [a, b, *]

[a] School of Mechanical and Manufacturing Engineering, University of New South Wales, Australia
[b] Australian Nuclear Science and Technology Organisation (ANSTO), Australia
[c] Los Alamos National Laboratory, New Mexico, USA

ARTICLE INFO

Article history:
Received 26 June 2019
Received in revised form
29 October 2019
Accepted 30 October 2019
Available online 5 November 2019

Keywords:
UO_2
ZrO_2
Thermal expansion
Thermal conductivity
Nuclear fuel

ABSTRACT

Molecular dynamics simulations were used to investigate the thermophysical properties of $(U,Zr)O_2$ between 300 K and 3500 K. For compositions with <25% UO_2 the tetragonal phase is stable and beyond 25% the cubic fluorite phase becomes stable for all temperatures. Thermal expansion, heat capacity and thermal conductivity have been predicted. The addition of ZrO_2 to UO_2 causes a reduction in thermal conductivity however this effect decreases with increased temperature and becomes insignificant beyond 1000 K. Thermal expansion of $(U,Zr)O_2$ mixtures with >25% UO_2, which are in the cubic fluorite phase, is similar to that of UO_2. A superionic transition is observed in cubic $(U,Zr)O_2$ at temperatures between 1500 K and 3000 K, occurring at progressively lower temperatures with increasing ZrO_2 content. The heat capacity of these mixed oxides increases from 80 J/mol.K up to 130 J/mol.K at temperatures relevant to accident conditions, possibly retarding temperature increase in fuels with a significant pellet-clad bonding layer.

1. Introduction

Light water reactors (LWRs) predominantly utilise UO_2 pellets as fuel [1]. UO_2 fuel pellets are often clad in zirconium based alloys to protect the fuel and to prevent radionuclides from being released into the coolant [1]. Zirconium alloys have been used as cladding materials since the early 1950s as they are corrosion resistant in water and have a small neutron absorption cross section [1].

Pellet cladding interaction (PCI) is a phenomenon found in nuclear reactors in which the fuel becomes mechanically and/or chemically bonded with its cladding material. PCIs affect the structural stability of both the fuel and the cladding, sometimes leading to the detrimental failure of the cladding [2]. When the cladding bonds with the fuel pellets a layer is formed that is composed of a solid solution of UO_2 and ZrO_2 in the full range of possible compositions across the layer [3]. PCIs are attributed with ~ 1% of cladding failure in pressurised water reactors and ~ 9% in boiling water reactors [2]. Failures induced by PCI occur in a small fraction of fuel rods, however, the chemical bonding occurs in the majority of commercial fuel rods [4–6].

The root cause of pellet clad bonding is oxidation of Zr caused by iodide (I^-) build-up in the pellet-cladding gap [4–6]. The initial formation of ZrO_2 allows a bond to form between the UO_2 fuel pellets and Zr alloy cladding. The stresses applied to the pellet-clad bonding layer during cooling or power ramps can lead to radial stresses on the pellet-clad bond, resulting in cracks [4–6]. Cracks are known to lead to an increase in iodide concentration at the cladding interface, which further exacerbates and accelerates the production of pellet-clad bonding [6].

Fuel burnup has risen from 15 GWd/t in the 1950s to over 50 GWd/t currently [7,8]. The incidence of pellet-clad bonding increases with burnup until, at 50 GWd/t, all fuel rods exhibit a chemical bonding between the fuel and cladding [3,9,10]. Beyond this, the ZrO_2 continues to leach into the fuel pellet and increases the thickness of the mixed oxide layer [3,9,10]. Reactor operators are attempting to reach higher burnups and are utilising fuel performance codes to simulate burnups over 100 GWd/t [11]. As the layer increases in thickness with burnup it becomes more important to the overall heat transfer coefficient with increased burnup. Burnup is currently on the cusp of permanent bonding, and as such the PCI bonding layer has not received the attention that perhaps it

* Corresponding author. School of Mechanical and Manufacturing Engineering, University of New South Wales, Australia.
E-mail address: p.burr@unsw.edu.au (P.A. Burr).

https://doi.org/10.1016/j.jnucmat.2019.151876
0022-3115/

deserves. The continued increase in burnup makes it prudent to investigate how this layer will affect the thermodynamics of nuclear fuel.

ZrO_2 exhibits several crystal structures depending on temperature and pressure. At atmospheric pressure, ZrO_2 is found in the monoclinic phase up to ~ 1420K, followed by the tetragonal phase to ~ 2620K and then the cubic phase until melting [12]. Cubic and tetragonal ZrO_2 are often stabilised using trivalent cations, of which Y_2O_3 is the most common, where ~ 2% Y_2O_3 is required for tetragonal stabilisation and ~ 8% is required for cubic stabilisation [13,14]. However, when looking at tetravalent dopants, such as CeO_2, it takes ~ 25% to stabilise ZrO_2 in the cubic phase [15,16].

ZrO_2 found in the pellet-clad bonding layers has been shown to be either cubic or tetragonally stabilised at room temperature, where, under out of pile conditions, the monoclinic phase is observed [12]. As burnup increases the tetragonal ZrO_2 is gradually replaced by cubic ZrO_2 and beyond 30GWd/t practically all ZrO_2 is cubic [3,9,10,17]. This stabilisation of both the cubic and tetragonal phases in nuclear fuel is due to a combination of factors including radiation damage, fission product dopants, accommodation of U in solid solution and stress induced stabilisation [9].

Past research on $(U,Zr)O_2$ has focussed on the phase diagram of the pellet-clad bonding material [18–22]. However, the thermophysical properties are still not well understood. Knowledge of thermal conductivity and heat capacity are useful in that they can be used to increase the accuracy of fuel centreline temperatures and heat transfer predictions [23,24]. Thermal expansion can be used to gauge how changes in temperature have the potential to cause cracking of fuel pellets at the pellet-clad interface. Mixed oxides sometimes have a minima in the melting point that is below both end members which could lead to localised melting at temperatures lower than expected [25].

Superionic conductivity is another phenomenon of interest that has been found to occur in UO_2 as well as several other actinide oxides [25–30]. ZrO_2 is often used with dopants to create low temperature superionic conductors, [31–34]. UO_2 is known to have a superionic transition at around 75% of its melting temperature [26–30,35]. Similarly, ZrO_2 undergoes a superionic transition at temperatures above 2500 K [31,33]. The effects that the addition of ZrO_2 to UO_2 will have on the superionic conductivity is explored in the current work.

The properties of the pellet-clad bonding layer are not currently accounted for in fuel performance codes [23,24]. This is partly due to the unavailability of data. In subsequent sections the thermophysical properties of cubic $(U,Zr)O_2$ are investigated along with those of tetragonal ZrO_2 using molecular dynamics (MD) simulations.

2. Methodology

2.1. Potential form

The Cooper-Rushton-Grimes (CRG) potential set, including interactions between Zr-O, Zr-Zr and Zr-U, were used for these simulations [29,36]. The CRG potential was chosen as it accurately reproduces the experimentally derived thermal expansion, bulk modulus and melting points of UO_2 and several mixed oxides containing UO_2 [29,30,35,37,38]. The CRG potential combines a pair potential with the embedded atom method (EAM) as per equation (1) [29,39]. This gives the potential energy of an atom i, E_i. Tables 1 and 2 contain the potential parameters used in all simulations taken from Cooper et al. and Liu et al. [29,36].

Table 1
Forcefield parameters for the pairwise interactions [29,36].

Interaction	$A_{\alpha\beta}$ (eV)	ϕ_β	$C_{\alpha\beta}$ (eV.Å^2)	$D_{\alpha\beta}$ (eV)	ϕ_M	r_0 (Å)
α-β		$\rho_{\alpha\beta}$ (Å)			$\gamma_{\alpha\beta}$ (Å^{-1})	
U - U	18600	0.2747	0.0	-	-	-
Zr - Zr	18600	0.2307	0.0	-	-	-
Zr - U	18600	0.2517	0.0	-	-	-
U - O	448.779	0.3878	0.0	0.6608	2.058	2.381
Zr - O	1147.471	0.3224	0.0	1.2269	1.4482	1.998
O - O	830.283	0.3529	3.8843	-	-	-

Table 2
Forcefield parameters for the many body interactions [29,36].

Species	G_α (eV.Å$^{1.5}$)	n_β (Å^5)
U	1.806	3450.995
Zr	1.597	1188.786
O	0.690	106.856

$$E_i = \frac{1}{2}\sum_j \phi_{\alpha\beta}(r_{ij}) - G_\alpha \sqrt{\sum_j \sigma_\beta(r_{ij})} \quad (1)$$

2.2. Simulation parameters

For all equilibrium simulations a Nosé-Hoover barostat and thermostat were used with the NPT (isothermal-isobaric) ensemble. The timestep, thermostat and barostat relaxation times were set to 2 fs, 0.1 ps and 0.5 ps, respectively. These values have been used widely in previous work that used the CRG potential [29,30,35,37,40]. Simulations were conducted for ZrO_2, $(Zr_{0.75},U_{0.25})O_2$, $(Zr_{0.50},U_{0.50})O_2$, $(Zr_{0.25},U_{0.75})O_2$ and UO_2.

2.2.1. Thermal expansion and heat capacity

Thermal expansion and heat capacity simulations were conducted for each composition. The tetragonal ZrO_2 $P42/nmc$ unit cell was repeated 12 times in each orthogonal direction to create a $12 \times 12 \times 12$ supercell (10368 atoms) [41]. All other structures consisted of a $10 \times 10 \times 10$ supercell (12000 atoms) of the cubic fluorite structure $Fm\bar{3}m$ [42].

Mixed oxide compositions were generated by randomly substituting U for Zr on cation sites. Due to the large number of atoms only one random arrangement of atoms was used for each composition. Previous work showed there to be minimal deviation between several random structures using 12000 atoms [30,35]. The pellet-clad layer is subject to continued ballistic intermixing during in-reactor operations and consequently no ordering is expected on the cation sublattice. This is in agreement with the TEM observations of Nogita et al. on the pellet-clad bonding layer of 48 GWd/t BWR samples [43]. Each supercell was heated from 300 K to 3500 K in 25 K increments. Each step consisted of a 20 ps ramp followed by a 20 ps equilibration. All results were calculated by taking the average over the final 4 ps of each equilibration step.

The cubic a lattice parameter was determined by taking the average of the unit cell length in the x, y and z directions. Similarly for the tetragonal structure the a lattice parameter was calculated from the average of the x and y simulation box dimensions, while the c parameter was taken from the z direction only. The thermal expansion coefficient (α_i) was determined, for isotropic materials, as $\alpha_V = \frac{1}{V}\left(\frac{\delta V}{\delta T}\right) = 3\alpha_i = \sum \frac{1}{L_i}\left(\frac{\delta L_i}{\delta T}\right)$ where V is volume [44]. For the

tetragonal structure the thermal expansion components in the *a* and *c* directions were calculated separately and the volumetric thermal expansion, α_V, was approximated as the trace of the tensor; $\alpha_V = 2\alpha_{11} + \alpha_{33}$ [44]. The derivative of the enthalpy increment as a function of temperature, $H(T) - H(T_{298})$, can be used to determine the specific heat capacity, $C_p = \frac{1}{n}\left(\frac{\delta H}{\delta T}\right)$, where n is the number of moles. For both heat capacity and thermal expansion the derivatives were calculated by taking a 3-point average before and after each point (± 25 K,± 50 K and ± 75 K) and using this in a central derivative.

2.3. Thermal conductivity

Thermal conductivity simulations utilised non-equilibrium molecular dynamics. The Müller-Plathe reverse perturbation method was utilised here [45]. This method involves swapping the kinetic energies of particles at the end of the supercell with those in the centre to generate a thermal gradient in the system. These simulations began by ramping to the desired temperature over a period of 20 ps followed by a 20 ps equilibration in an NPT ensemble. Following this an NVE ensemble (isochoric-isenthalpic) is used over a period of 5 ns, during which the Müller-Plathe function is used. 5 ns was used as it ensured that the thermal conductivity and heat flux had converged, see supplementary materials.

Thermal conductivity, k_i, is then calculated as per equations (2) and (3), where J_i is the heat flux, q_i is the energy that has been transferred between atoms, L_i is the supercell length in the i direction, A is the area of the supercell, ΔT is the thermal gradient and t is the simulation time. As the centre of the box is the point to which energy is transferred the thermal gradient acts over two halves ($\frac{L_i}{2}$) and acts over twice the area ($2A$).

$$k_i = J_i\left(\frac{L_i}{2\Delta T}\right) \tag{2}$$

$$J_i = \frac{q_i}{2At} \tag{3}$$

Bulk thermal conductivity was calculated by extrapolating from the thermal conductivity for several supercell sizes. This was done for a $5 \times 5 \times 20$, a $5 \times 5 \times 40$ and a $5 \times 5 \times 60$ supercell for each composition. The bulk value was determined by fitting a straight line to $\frac{1}{k_i}$ as a function of $\frac{1}{z}$ and extrapolating to an infinite cell, see supplementary materials for details. For tetragonal ZrO_2 the thermal conductivity was calculated in the *a* and *c* directions.

3. Results and discussion

Upon modelling the pure ZrO_2 phases it appears that the Zr-O CRG potential correctly predicts the tetragonal phase of ZrO_2, however, fails to predict the monoclinic and cubic phases, unless dopants are introduced. The inability to model the monoclinic phase was reported previously and is attributed to the centro-symmetric form of the potential [36]. Previous work observed a tetragonal to cubic phase transition, but, when we were attempting to simulate the cubic phase, the structure collapsed into a parasitic phase that does not represent any known phase of ZrO_2 [12,36]. The model also predicted that upon the addition of >25% UO_2 to ZrO_2 the cubic phase becomes stable at all temperatures, similar to the amount required for other tetravalant cations in ZrO_2 [15,16]. The potential predicts good agreement with literature regarding the stabilisation of ZrO_2 using tetravalent dopants [15,16].

Whilst the melting point of the UO_2 end member is within 100 K of experimental measurements, the melting temperatures of the $(U,Zr)O_2$ mixtures were unable to be accurately predicted and the results are available in the supplementary materials. The melting points of the $(U,Zr)O_2$ mixtures do not follow the trend found in experimental results [22,46]. The accuracy of the melting point prediction decreases as ZrO_2 content is increased, partly due to the inability to accurately predict the melting point of the ZrO_2 end member due to the aforementioned parasitic phase.

3.1. Thermal expansion

The lattice parameter as a function of temperature and composition is shown in Fig. 1. Fig. 1a shows the lattice parameters of the cubic phase $(U,Zr)O_2$ and UO_2, Fig. 1b shows the tetragonal lattice parameters of ZrO_2 up to 1800 K, beyond which it transforms into the parasitic phase. The lattice parameters for both end members agree closely with the literature. For UO_2, $(U_{0.75},Zr_{0.25})O_2$ and $(U_{0.50},Zr_{0.50})O_2$ an inflection occurs in the lattice parameter at temperatures >2000 K. For UO_2 it has been previously reported that this inflection coincides with a disorder of the oxygen sublattice, otherwise known as an superionic transition [26–30]. $(U_{0.25},Zr_{0.75})O_2$ also exhibits the same inflection at ~ 1800 K, however the inflection is in the opposite direction (a reduction in lattice expansion for ~ 50 K).

The temperature at which the superionic transition occurs and the magnitude of the increase in the thermal expansion also appear to be dependant on the Zr content of the solid solution, with increasing Zr content causing a decrease in both the transition temperature and the rate of thermal expansion. This is shown more clearly in Fig. 2. The peak in thermal expansion associated with $(U,Zr)O_2$ with >50% UO_2 is inversed for the composition $(U_{0.25},Zr_{0.75})O_2$. Thus indicating that Zr rich $(U,Zr)O_2$ exhibits a reduction in the rate of thermal expansion between 1800 and 2100 K, although it should be noted that the thermal expansion remains positive. The thermal expansion of $(U_{0.25},Zr_{0.75})O_2$ and ZrO_2 diverge from that of $(U,Zr)O_2$ with >50% UO_2 at 1200 K and 700 K respectively.

Thermal expansion measured by Haggerty et al. for t-ZrO_2 decreased between 1170 K and 1470 K followed by a slight increase until 1770 K [51]. Although both our results and those of Haggerty et al. show nearly constant thermal expansion for t-ZrO_2, caution should be used when using this potential set to predict the thermal expansion of Zr-rich compounds given the discrepancy of ~27% in absolute thermal expansion values. However, as the rates of thermal expansion have a similar trend it is possible to draw some conclusions on how the rate of change in thermal expansion could affect the pellet-clad bonding. Both our predictions and the measurements of Haggerty et al. show that the thermal expansion in the *c* direction reduces with increasing temperature, whilst the *a* thermal expansion increases as the structure moves towards the cubic phase [51] (see supplementary materials).

Given the significant difference in the rates of thermal expansion between tetragonal ZrO_2 and the cubic $(U,Zr)O_2$ phase, at temperatures exceeding 1000 K, there is a high potential for cracking in the lattice as it cools after being heated rapidly in the case of a power ramp. As tetragonal ZrO_2 is observed in fuel with burnups of less than 30 GWd/t the difference in thermal expansion rates could be a factor in cracking at the PCI interface [9,10,17]. On the other hand, cubic Zr-rich compositions of $(U,Zr)O_2$ are unlikely to generate sufficient strain to induce cracking as the divergence of thermal expansion occurs at temperatures greater than that seen at the pellet-clad interface.

The presence of an early-onset superionic transition in Zr-rich $(U,Zr)O_2$ is further evidenced by examining the O-O pairwise radial distribution function of $(U_{0.25},Zr_{0.75})O_2$, shown in Fig. 3a. It is

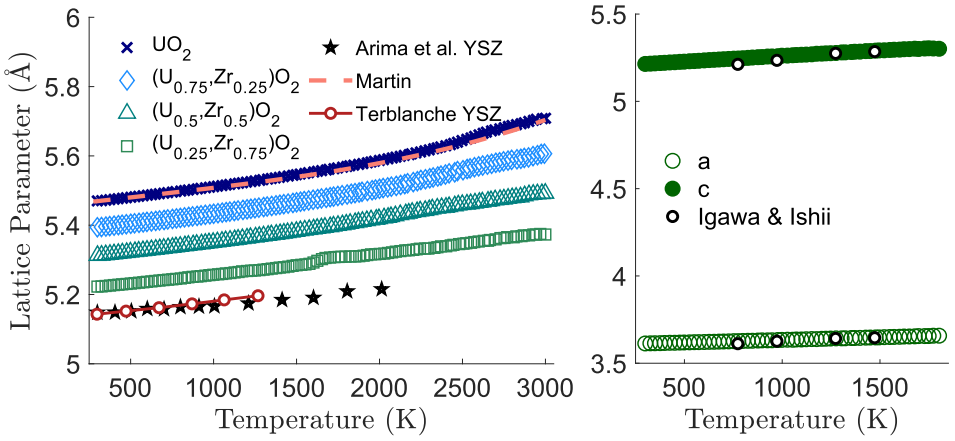

Fig. 1. Lattice parameter of (a) cubic UO_2, (U,Zr)O_2 and (b) tetragonal ZrO_2 as a function of temperature compared with experimental [47–49] and previous MD literature values [50].

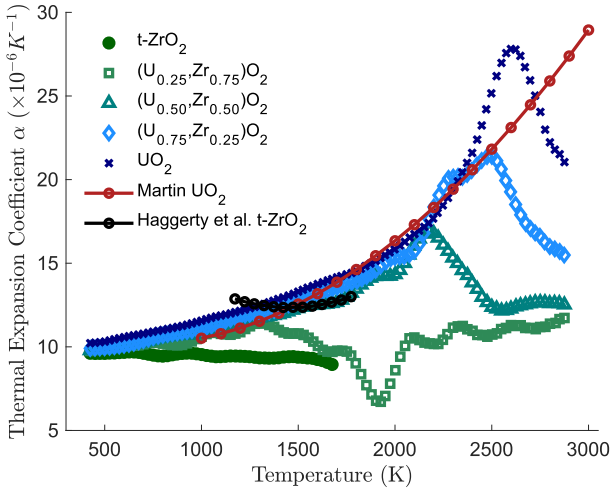

Fig. 2. The thermal expansion coefficients as a function of temperature and composition compared with experiments [47,51]. Note that the coefficient for tetragonal ZrO_2 is the volumetric coefficient.

apparent that there is a loss of all peaks beyond the first nearest neighbour above 1500 K, consistent with disorder in the oxygen sublattice. Additionally, Fig. 3b shows that the cation sites maintain structure at the superionic transition temperature and above, with peak broadening due to increased thermal vibrations. This analysis of the superionic transition can not be done for pure ZrO_2 as the potential is unable to predict the cubic phase without the addition of dopants.

3.2. Heat capacity and melting point

The predicted specific heat capacity as a function of temperature for each composition can be seen in Fig. 4. Heat capacity increases linearly and approximately equally with temperature for all compositions below 1700 K. The predicted heat capacity for both UO_2 and ZrO_2 show good agreement with the literature [27,52–55]. The predictions do not replicate the peak caused by the monoclinic to tetragonal transition that occurs at ~1470 K in ZrO_2. $(U_{0.25},Zr_{0.75})O_2$, $(U_{0.50},Zr_{0.50})O_2$, $(U_{0.75},Zr_{0.25})O_2$ and UO_2 exhibit a steep increase in the heat capacity at 1800 K, 2000 K, 2300 K and 2500 K respectively. This correlates with the previously mentioned superionic transition temperatures. Higher concentrations of UO_2 exhibit a shift in superionic transition peaks towards higher temperatures. The increased heat capacity at the superionic transition temperature, seen in Fig. 4, is due to the increase in concentration of defects being created in the oxygen sublattice [27,30,35].

At operating temperatures the heat capacity is fairly constant for all compositions examined here. However, under accident conditions the sharp increases in heat capacity of the Zr-rich (U,Zr)O_2 mixtures at lower temperatures than for UO_2 could result in delayed heating of fuel containing a permanently bonded (U,Zr)O_2 layer compared to fresh fuel. This suggests that high burnup fuels, > 50 GWd/t, which contains the greatest fraction of (U,Zr)O_2 layer has

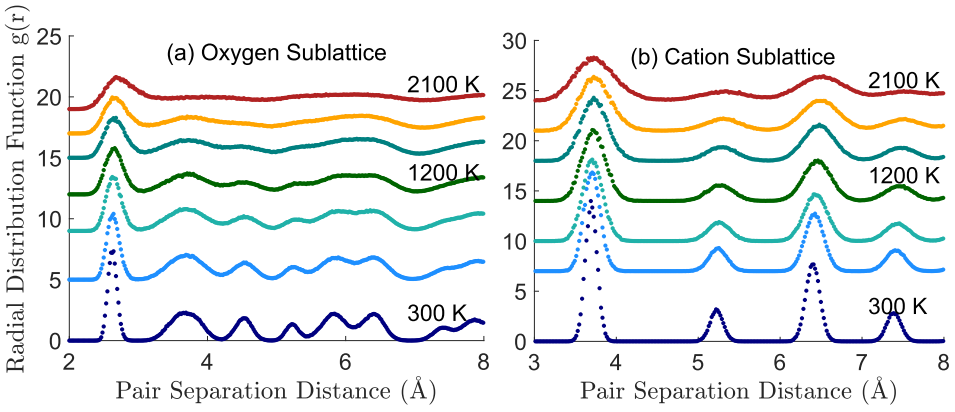

Fig. 3. Radial distribution function (RDF) of (a) oxygen and (b) cation sublattices from 300 to 2100 K in increments of 300 K.

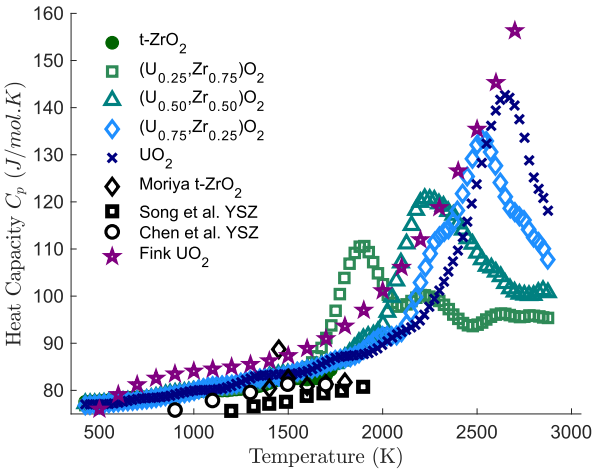

Fig. 4. Heat capacity as a function of composition and temperature [27,52–54].

an inherent mechanism to delay temperature increases in fuel during accident scenarios. This may partly compensate for the reduced thermal conductivity of high burnup microstructures.

3.3. Thermal conductivity

The thermal conductivity of UO_2 and (U,Zr)O_2 are shown in Fig. 5a and for ZrO_2 in Fig. 5b. MD alone tends to overestimate thermal conductivity at low temperatures as it doesn't include spin-phonon scattering contributions [56]. However, at high temperature these become negligible, and a good agreement between MD and experiments is observed at temperatures exceeding 1000 K [27,37,56]. Differences between this work and earlier work using the CRG potential to determine thermal conductivity of UO_2, at low temperatures, are attributed to differing cell sizes used to determine the bulk values. The largest supercell used by Cooper et al. was $10 \times 10 \times 60$ compared to the $5 \times 5 \times 60$ supercell used here. This had a marked effect at room temperature but came within uncertainty bounds of the current and previous work.

The thermal conductivity of zirconia, Fig. 5b, shows a similar trend seen in UO_2, where predicted thermal conductivity of ZrO_2 deviates from experimentally derived results for YSZ at low temperatures [57,58]. Accounting for phonon-spin scattering would result in improved accuracy of thermal conductivity predictions as seen by Cooper et al. [56]. The lower thermal conductivity in the z direction could be a function of the anharmonicity of phonon scattering found in tetragonal ZrO_2 [59]. Where the composition of (U,Zr)O_2 contains > 25% UO_2 the thermal conductivities are similar to those of UO_2. At typical cladding interface temperatures ~ 625 K the bonding layer would have a negligible impact on the thermal conductivity of the fuel compared to fresh fuel.

At burnups less than 30 GWd/t, where ZrO_2 remains tetragonal, our predictions show a limited difference between ZrO_2 and the mixed oxides. The effect of differences in the thermal conductivities would have little impact on overall heat transfer. The mixed oxide layer has similar predicted thermal conductivity to that of the fuel. In fact, due to bonding, the thermal conductivity would likely be better than in fresh fuel as the bonding layer has significantly higher thermal conductivity than the He and fission product gases, if the inclusion of cracks are ignored [60]. It is, however, recommended to include the formations of ZrO_2 and the (U,Zr)O_2 with distinct thermal properties in a gap evolution model used by fuel performance codes, mainly due to the thermal degradation caused by tetragonal ZrO_2. Table 3 contains predicted properties of (U,Zr)O_2 at standard temperature and pressure along with selected literature values for comparison. The uncertainty in the results is the standard deviation over the averaging window (final 4 ps per temperature step).

4. Conclusion

Thermophysical properties of urania-zirconia mixed oxides

Table 3
Calculated lattice parameters, a and c, thermal expansion coefficient (α_v), heat capacity (C_p) and thermal conductivity (κ_c) at 300 K and 1 atm.

Composition	a	c	α_v	C_p	κ_c
	Å	Å	K^{-1}	J/mol.K	W/m.K
ZrO_2	3.613 ± 0.002	5.214 ± 0.002	9.59 ± 0.11	77.3 ± 0.9	6.0
ZrO_2 Exp.	$(3.596)^a$	$(5.177)^a$	$(9.72)^b$	$(60.4)^c$	$(3.1)^d$
$U_{0.25}Zr_{0.75}$	5.228 ± 0.001		9.66 ± 0.10	77.4 ± 0.7	9.37
$U_{0.50}Zr_{0.50}$	5.312 ± 0.001		9.75 ± 0.10	77.0 ± 0.7	10.77
$U_{0.75}Zr_{0.25}$	5.394 ± 0.001		9.87 ± 0.10	76.4 ± 0.8	12.57
UO_2	5.469 ± 0.001		10.16 ± 0.11	76.9 ± 0.8	21.94
UO_2 Exp.	$(5.468)^e$		$(10.56)^e$	$(75.0)^e$	$(7.59)^e$

a – Lutterotti et al. [61].
b – Terblanche et al. [49].
c – Tojo et al. [55].
d – Hasselman et al. [62].
e – Fink [27].

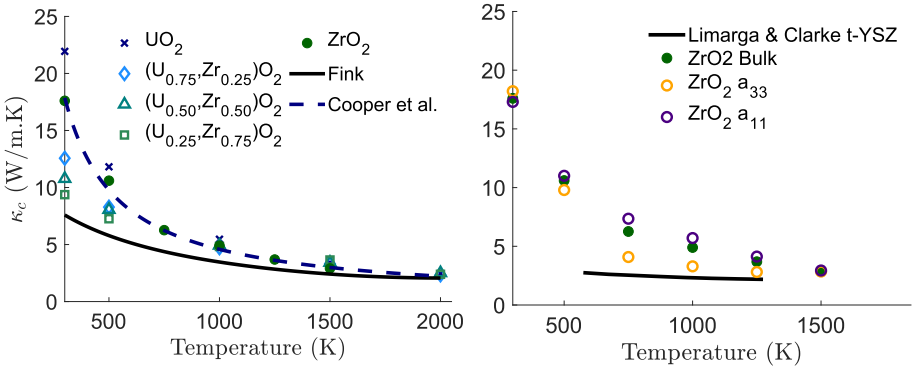

(a) Thermal conductivity for UO_2, bulk ZrO_2 and all mixed oxides [27, 37].

(b) Thermal conductivity for tetragonal phase zirconia [57, 58].

Fig. 5. The predicted thermal conductivity as a function of temperature and composition.

have been modelled using MD. The simulations predict the properties of the end members' with a high degree of accuracy, including the lattice parameter, heat capacity and thermal conductivity. Following this, the properties of mixed $(U,Zr)O_2$, which are commonly found in high burnup nuclear fuels, have been predicted.

At temperatures below 1800 K, the predicted thermal expansion coefficient of tetragonal ZrO_2 is lower than that of all compositions of cubic $(U,Zr)O_2$. The cubic $(U,Zr)O_2$ mixtures have very similar thermal expansion to that of UO_2 until they reach their superionic transition temperature. The results indicate that adding ZrO_2 to UO_2 causes a shift in the superionic transition to lower temperatures. This is evidenced by changes in thermal expansion, disorder of the oxygen sublattice and increases in heat capacity caused by the increased concentration of oxygen defects. The heat capacity and thermal expansion peaks occur at temperatures up to 1000 K lower for $(U_{0.25},Zr_{0.75})O_2$ than for UO_2.

The thermal conductivity of cubic $(U,Zr)O_2$ was found to be very similar to that of UO_2, especially beyond 1000 K. The formation of tetragonal ZrO_2, associated with burnups <30 GWd/t, does not impede heat transfer. However, at temperatures close to room temperature the formation of cubic $(U,Zr)O_2$ compounds, associated with high burn-up, results in a reduction in thermal conductivity compared to either end member, with this difference reducing as temperature increases.

Acknowledgements

This work was supported by the MASSIVE HPC facility (www.massive.org.au). This work was also supported by the assistance and services from the National Computational Infrastructure (NCI), which is supported by the Australian Government and this work utilised the resources of the Pawsey Supercomputing Centre (www.pawsey.org.au). The authors would like to thank the Australian Institute of Nuclear Science and Engineering (AINSE Limited) for providing financial assistance (Residential Student Scholarship Award ALNSTU12411) to enable work on this project. This research was supported by an Australian Government Research Training Program (RTP) Scholarship. Funding for MWDC was provided by the U.S. Department of Energy, Office of Nuclear Energy, Nuclear Energy Advanced Modeling and Simulations (NEAMS) program. Los Alamos National Laboratory, an affermative action/equal opportunity employer, is operated by Triad National Security, LLC, for the National Nuclear Security Administration of the U.S. Department of Energy under Contract No. 89233218CNA000001. Dr. Jessica Carolan-Veliscek is thanked for her assistance.

Appendix A. Supplementary data

Supplementary data to this article can be found online at https://doi.org/10.1016/j.jnucmat.2019.151876.

Data availability

The raw and processed data required to reproduce these findings are available to download from https://doi.org/10.26190/5d1d47a9eb76f.

References

[1] IAEA, Thermophysical properties of materials for nuclear engineering: a tutorial and collection of data, Tech. Rep. (2008).
[2] IAEA, Review of fuel failures in water cooled reactors, IAEA Nuclear Energy Series (2010) 1–171.
[3] K.T. Kim, UO_2/Zry-4 chemical interaction layers for intact and leak PWR fuel rods, J. Nucl. Mater. 404 (2010) 128–137.
[4] S.P. Walker, A. Yu, R.T. Fenner, Pellet-clad mechanical interaction: pellet-clad bond failure and strain relief, Nucl. Eng. Des. 138 (1992) 403–408.
[5] S.P. Ayu, R.T. Walker, Fenner, Pellet-clad bonding during PCMI, Nucl. Eng. Des. 121 (1990) 53–58.
[6] B. Cox, Pellet-clad interaction (PCI) failures of zirconium alloy fuel cladding - a review, J. Nucl. Mater. 172 (1990) 249–292.
[7] J. Kim, H. Yoon, D. Kook, Y. Kim, A study on the initial characteristics of domestic spent nuclear fuels for long term dry storage, Nuclear Engineering and Technology 45 (2013) 377–384.
[8] IAEA, Energy, electricity and nuclear power estimates for the period up to 2050 Reference Data Series 1, Tech. Rep. (2014).
[9] K. Nogita, K. Une, Formation of pellet-cladding bonding layer in high burnup BWR fuels, J. Nucl. Sci. Technol. 34 (1997) 679–686.
[10] S. Van den Berghe, A. Leenaers, B. Vos, L. Sannen, M. Verwerft, Observation of a pellet-cladding bonding layer in high power fuel, in: Adv. Fuel Pellet Materials and Designs for Water Cooled Reactors, 2003, pp. 265–272.
[11] OECD/NEA, Technology Roadmap Update for Generation IV Nuclear Energy Systems, Preparing Today for Tomorrow's Energy Needs, 2014, p. 7.
[12] L.G. Liu, New high pressure phases of ZrO_2 and HfO_2, J. Phys. Chem. Solids 41 (1980) 331–334.
[13] D. Wang, Y. Guo, K. Liang, K. Tao, Crystal structure of zirconia by Rietveld refinement, Sci. China, Ser. A: Mathematics, Physics, Astronomy 42 (1999) 80–86.
[14] J.R. Kelly, I. Denry, Stabilized zirconia as a structural ceramic: an overview, Dent. Mater. 24 (2008) 289–298.
[15] J.R. Brandon, R. Taylor, Thermal properties of ceria and yttria partially stabilized zirconia thermal barrier coatings, Surf. Coat. Technol. 39–40 (1989) 143–151.
[16] S.Y. Park, J.H. Kim, M.C. Kim, H.S. Song, C.G. Park, Microscopic observation of degradation behavior in yttria and ceria stabilized zirconia thermal barrier coatings under hot corrosion, Surf. Coat. Technol. 190 (2005) 357–365.
[17] R.M. Berman, Homogeinization of two-phase mixture of ZrO_2-UO_2 by irradiation, J. Nucl. Mater. 17 (1965) 313–323.
[18] K. Romberger, C. Baes, H. Stone, Phase equilibrium studies in the UO_2-ZrO_2 system, J. Inorg. Nucl. Chem. 29 (2003) 1619–1630.
[19] P.E. Evans, The system UO_2-ZrO_2, J. Am. Ceram. Soc. 43 (2006) 443–446.
[20] S. Aronson, J.C. Clayton, Thermodynamic properties of nonstoichiometric Urania-Zirconia solid solutions, J. Chem. Phys. 35 (1961) 1055–1058.
[21] M. Yashima, T. Koura, Y. Du, M. Yoshimura, Thermodynamic assessment of the zirconia-urania system, J. Am. Ceram. Soc. 79 (1996) 521–524.
[22] S. Mastromarino, A. Seibert, E. Hashem, A. Ciccioli, D. Prieur, A. Scheinost, S. Stohr, P. Lajarge, J. Boshoven, D. Robba, M. Ernstberger, D. Bottomley, D. Manara, Assessment of solid/liquid equilibria in the $(U,Zr)O_{2+y}$ system, J. Nucl. Mater. 494 (2017) 368–379.
[23] G. Rossiter, I. Palmer, R. Gregg, Development of the ENIGMA fuel performance code, NNL science (2013) 24–27.
[24] J.D. Hales, R.L. Williamson, S.R. Novascone, G. Pastore, B. Spencer, D. Stafford, K.A. Gamble, D.M. Perez, R.J. Gardner, W. Liu, J. Galloway, C. Matthews, C. Unal, N. Carlson, BISON Theory Manual the Equations behind Nuclear Fuel Analysis, vol. 3, 2016, pp. 15–142.
[25] P.S. Ghosh, N. Kuganathan, C.O.T. Galvin, A. Arya, G.K. Dey, B.K. Dutta, R.W. Grimes, Melting behavior of $(Th,U)O_2$ and $(Th,Pu)O_2$ mixed oxides, J. Nucl. Mater. 479 (2016) 112–122.
[26] C.T. Walker, M. Coquerelle, W. Goll, R. Manzel, Irradiation behaviour of MOX fuel: results of an EPMA investigation, Nucl. Eng. Des. 131 (1991) 1–16.
[27] J.K. Fink, Thermophysical properties of uranium dioxide, J. Nucl. Mater. 279 (2000) 1–18.
[28] C. Ronchi, M. Sheindlin, M. Musella, G.J. Hyland, Thermal conductivity of uranium dioxide up to 2900 K from simultaneous measurement of the heat capacity and thermal diffusivity, J. Appl. Phys. 85 (1999) 776–789.
[29] M.W.D. Cooper, M.J.D. Rushton, R.W. Grimes, A many-body potential approach to modelling the thermomechanical properties of actinide oxides, J. Phys. Condens. Matter 26 (2014).
[30] C.O.T. Galvin, M.W.D. Cooper, M.J.D. Rushton, R.W. Grimes, Thermophysical properties and oxygen transport in $(Th_x,Pu_{1-x})O_2$, Sci. Rep. 6 (2016) 1–10.
[31] P. Aldebert, J. Traverse, Structure and ionic mobility of zirconia at high temperature, Chemischer Informationsdienst 16 (1985) 34–40.
[32] M. Sillassen, P. Eklund, N. Pryds, E. Johnson, U. Helmersson, J. Bøttiger, Low-temperature superionic conductivity in strained yttria-stabilized zirconia, Adv. Funct. Mater. 20 (2010) 2071–2076.
[33] A. Eichler, Tetragonal Y-doped zirconia: structure and ion conductivity, Phys. Rev. B Condens. Matter Mater. Phys. 64 (2001) 1–8.
[34] N. Mahato, A. Banerjee, A. Gupta, S. Omar, K. Balani, Progress in material selection for solid oxide fuel cell technology: a review, Prog. Mater. Sci. 72 (2015) 141–337.
[35] M.W.D. Cooper, S.T. Murphy, M.J.D. Rushton, R.W. Grimes, "Thermophysical properties and oxygen transport in the $(U_x,Pu_{1-x})O_2$ lattice, J. Nucl. Mater. 461 (2015) 206–214.
[36] X.Y. Liu, M.W.D. Cooper, K.J. McClellan, J.C. Lashley, D.D. Byler, B.D.C. Bell, R.W. Grimes, C.R. Stanek, D.A. Andersson, Molecular dynamics simulation of thermal transport in UO_2 containing uranium, oxygen, and fission-product defects, Physical Review Applied 6 (2016), 044015.
[37] M. Cooper, S. Middleburgh, R. Grimes, "Modelling the thermal conductivity of $(U_xTh_{1-x})O_2$ and $(U_xPu_{1-x})O_2$, J. Nucl. Mater. 466 (2015) 29–35.
[38] M.W.D. Cooper, N. Kuganathan, P.A. Burr, M.J.D. Rushton, R.W. Grimes,

C.R. Stanek, D.A. Andersson, Development of Xe and Kr empirical potentials for CeO_2, ThO_2, UO_2 and PuO_2, combining DFT with high temperature MD, J. Phys. Condens. Matter 28 (40) (2016).
[39] M.S. Daw, S.M. Foiles, M.I. Baskes, The embedded-atom method: a review of theory and applications, Mater. Sci. Rep. 9 (1993) 251–310.
[40] M.J. Qin, M.W.D. Cooper, E.Y. Kuo, M.J.D. Rushton, R.W. Grimes, G.R. Lumpkin, S.C. Middleburgh, Thermal conductivity and energetic recoils in UO_2 using a many-body potential model, J. Phys. Condens. Matter 26 (2014).
[41] J. Málek, L. Beneš, T. Mitsuhashi, Powder diffraction data and Rietveld refinement of metastable t-ZrO_2 at low temperature, Powder Diffr. 12 (1997) 96–98.
[42] L. Desgranges, G. Baldinozzi, G. Rousseau, J.C. Nièpce, G. Calvarin, Neutron diffraction study of the in situ oxidation of UO2, Inorg. Chem. 48 (2009) 7585–7592.
[43] K. Nogita, K. Une, Y. Korei, TEM analysis of pellet-cladding bonding layer in high burnup BWR fuel, Nucl. Instrum. Methods Phys. Res. Sect. B Beam Interact. Mater. Atoms 116 (1996) 521–526.
[44] J.H. Robertson, Physical Properties of Crystals: Their Representation by Tensors and Matrices, 41, Oxford University Press, Clarendon Press, 2009.
[45] F. Müller-Plathe, A simple nonequilibrium molecular dynamics method for calculating the thermal conductivity, J. Chem. Phys. 106 (1997) 6082–6085.
[46] W.A. Lambertson, M.H. Mueller, Uranium oxide phase equilibrium systems: III, UO_2-ZrO_2, J. Am. Ceram. Soc. 36 (1953) 365–368.
[47] D.G. Martin, The thermal expansion of solid UO_2 and (U, Pu) mixed oxides - a review and recommendations, J. Nucl. Mater. 152 (1988) 94–101.
[48] N. Igawa, Y. Ishii, Crystal structure of metastable tetragonal zirconia up to 1473 K, J. Am. Ceram. Soc. 84 (2001) 1169–1171.
[49] S.P. Terblanche, Thermal-expansion coefficients of yttria-stabilized cubic zirconias, J. Appl. Crystallogr. 22 (1989) 283–284.
[50] T. Arima, K. Fukuyo, K. Idemitsu, Y. Inagaki, Molecular dynamics simulation of yttria-stabilized zirconia between 300 and 2000 K, J. Mol. Liq. 113 (1) (2004) 67–73.
[51] R.P. Haggerty, P. Sarin, Z.D. Apostolov, P.E. Driemeyer, W.M. Kriven, Thermal expansion of HfO_2 and ZrO_2, J. Am. Ceram. Soc. 97 (2014) 2213–2222.
[52] X. Song, M. Xie, F. Zhou, G. Jia, X. Hao, S. An, High-temperature thermal properties of yttria fully stabilized zirconia ceramics, J. Rare Earths 29 (2) (2011) 155–159.
[53] M. Chen, B. Hallstedt, L.J. Gauckler, Thermodynamic Modeling of the ZrO_2-$YO_{1.5}$ System, 170, 2004, pp. 255–274.
[54] Y. Moriya, A. Navrotsky, "High-temperature calorimetry of zirconia: heat capacity and thermodynamics of the monoclinic–tetragonal phase transition, J. Chem. Thermodyn. 38 (2006) 211–223.
[55] T. Tojo, T. Atake, T. Mori, H. Yamamura, Heat capacity and thermodynamic functions of zirconia and yttria-stabilized zirconia, J. Chem. Thermodyn. 31 (1999) 831–845.
[56] M.W.D. Cooper, C.R. Stanek, X.Y. Liu, D.A. Andersson, A comment on the thermal conductivity of (U,Pu)O_2 and (U,Th)O_2 by molecular dynamics with adjustment for phonon-spin scattering, MRS Advances 1 (2016) 2483–2487.
[57] A.M. Limarga, D.R. Clarke, The grain size and temperature dependence of the thermal conductivity of polycrystalline, tetragonal yttria-stabilized zirconia, Appl. Phys. Lett. 98 (2011), 211906.
[58] A.M. Limarga, S. Shian, M. Baram, D.R. Clarke, Effect of high-temperature aging on the thermal conductivity of nanocrystalline tetragonal yttria-stabilized zirconia, Acta Mater. 60 (2012) 5417–5424.
[59] C.W. Li, H.L. Smith, T. Lan, J.L. Niedziela, J.A. Muñoz, J.B. Keith, L. Mauger, D.L. Abernathy, B. Fultz, Phonon anharmonicity of monoclinic zirconia and yttrium-stabilized zirconia, Phys. Rev. B Condens. Matter Mater. Phys. 91 (2015), 144302.
[60] H. Petersen, The properties of helium: density, specific heats, viscosity, and thermal conductivity at pressures from 1 to 100 bar and from room temperature to about 1800 K, Tech. Rep. (1970).
[61] L. Lutterotti, P. Scardi, Simultaneous structure and size-strain refinement by the rietveld method, J. Appl. Crystallogr. 23 (4) (1990) 246–252.
[62] D.P. Hasselman, L.F. Johnson, L.D. Bentsen, R. Syed, H.L. Lee, M.V. Swain, Thermal diffusivity and conductivity of dense polycrystalline ZrO_2 ceramics a survey, Am. Ceram. Soc. Bull. 66 (1987) 799–806.